Nanoscale

PAPER

View Article Online
View Journal | View Issue

Cite this: *Nanoscale*, 2024, **16**, 21388

Recognizing the reactive sites of $SnFe_2O_4$ for the oxygen evolution reaction: the synergistic effect of Sn^{II} and Fe^{III} in stabilizing reaction intermediates†

Anubha Rajput,[a] Pandiyan Sivasakthi,[b] Pralok K. Samanta *[b] and Biswarup Chakraborty *[a]

Among the reported spinel ferrites, the p-block metal containing $SnFe_2O_4$ is scarcely explored, but it is a promising water-splitting electrocatalyst. This study focuses on the reaction kinetics and atomic scale insight of the reaction mechanism of the oxygen evolution reaction (OER) catalyzed by $SnFe_2O_4$ and analogous Fe_3O_4. The replacement of Fe^{II}_{Oh} sites with Sn^{II}_{Oh} in $SnFe_2O_4$ improves the catalytic efficiency and various intrinsic parameters affecting the reaction kinetics. The variable temperature OER depicts a low activation energy (E_a) of 28.71 kJ mol^{-1} on $SnFe_2O_4$. Experimentally determined second-order dependence on [OH^-] and the prominent kinetic isotope effect observed during the deuterium labelling study implies the role of hydroxide ions in the rate-determining step (RDS). Using density functional theory, the reaction mechanism on the (001) surface of $SnFe_2O_4$ and Fe_3O_4 is modelled. The DFT simulated free energy diagram for the reaction intermediates shows an adsorbate evolution mechanism (AEM) on both the ferrites' surfaces where the formation of *OOH is the RDS on $SnFe_2O_4$ while *O formation is the RDS on Fe_3O_4. In contrast to other spinel ferrites, where individual metal sites act independently, in case of $SnFe_2O_4$, a synergy between Fe^{III}_{Oh} and the neighbouring Sn^{II}_{Oh} atoms is responsible for stabilizing the OER intermediates, enhancing the catalytic OER activity of $SnFe_2O_4$ as compared to isostructural Fe_3O_4.

Received 28th July 2024,
Accepted 20th October 2024

DOI: 10.1039/d4nr03107e

rsc.li/nanoscale

Introduction

Spinel oxides with a common formula AB_2O_4 exhibit a cubic close-packed lattice with two basic crystallographic sites, namely octahedral (Oh) and tetrahedral (Td) sites. The normal spinel has a configuration of $A^{II}_{Td}(B^{III}_{Oh})_2O_4$ where A^{2+} ions occupy the tetrahedral sites, while B^{3+} ions occupy the octahedral sites, whereas in an inverse spinel with a configuration of $B^{III}_{Td}(A^{II}_{Oh}B^{III}_{Oh})O_4$, the divalent cations occupy half of the octahedral sites.[1] The presence of mixed-valence cations with accessible multiple redox states results in high electronic conductivity, favourable for electrocatalytic OER performance.[2] In the last decade, cobaltite spinel-oxide MCo_2O_4 materials (M = Mn, Co, Ni, Zn, *etc.*) were explored as the anode material for the OER and the Co_{Oh} sites were believed to be the reactive sites for the OER.[3–5] The inverse-spinel Fe_3O_4 and metal ferrites such as $NiFe_2O_4$ and $CoFe_2O_4$ nanoparticles also exhibit remarkable OER activity.[6] Bimetallic spinel ferrites have been shown to outperform their monometallic counterparts toward the OER.[7] To manifest the experimental difference in the catalytic activity of the bimetallic and monometallic catalysts, computational modelling and an atomistic level understanding of the reaction mechanism are crucial. Theoretical studies performed with $NiFe_2O_4$ identified that the nickel sites exposed on the (001) plane are active for the OER and follow a lattice oxygen mechanism (LOM).[6] However, on the (001) surface of $CoFe_2O_4$, both the cobalt and iron sites participate independently in the OER as individual reactive sites following the adsorbate evolution mechanism (AEM).[6] In general, due to poor covalency between the transition metal and oxygen, the OER on the spinel oxides follows the AEM.[8] However, a recent experimental study revealed the LOM as the dominant pathway of the OER on $NiFe_2O_4$.[9] Tin ferrite ($SnFe_2O_4$) is another important metal ferrite spinel that has been recently reported as a bi-functional electrode material to perform electrochemical water splitting at very low overpotentials.[10] The $SnFe_2O_4$ lattice exhibits three potent catalytic sites *viz.* Sn^{II}_{Oh}, Fe^{III}_{Td}, and Fe^{III}_{Oh}, out of which Fe^{3+} sites were predicted to facilitate the OER. However, to uncover the real OER mechanism and to determine the possible effect of heteroatom doping, a detailed electro-kinetics and computational study is very important.

[a]*Department of Chemistry, Indian Institute of Technology Delhi, Hauz Khas, 110016 New Delhi, India. E-mail: cbiswarup@chemistry.iitd.ac.in*
[b]*Department of Chemistry, Birla Institute of Technology and Science Pilani (BITS Pilani), Hyderabad Campus, Hyderabad-500078, India. E-mail: pralokkumar.samanta@hyderabad.bits-pilani.ac.in*

†Electronic supplementary information (ESI) available. See DOI: https://doi.org/10.1039/d4nr03107e

To validate the experimentally obtained electro-kinetic data (intrinsic reaction parameters) and to understand the reaction mechanism of the OER, theoretical studies are also important. Recently, Goddard's group proposed that during the OER, Fe^{IV} and Ni^{IV} synergistically act in stabilizing the reaction intermediates, to impart excellent activity to NiFe(O)OH.[11] Temperature-dependent and electrolyte concentration-dependent electrokinetics on NiFe LDH studied by Hu and co-workers also yielded several intrinsic parameters.[12] Carter and co-workers also studied the effect of temperature on the activity of NiFe(O)OH, with a hundred-fold increase in the catalytic current at a fixed potential.[13] Driess's group substituted Co^{II} with redox inactive Zn^{II} in Co_3O_4 and found that Zn^{II} stabilized Co^{IV}, which are the main active sites during the OER.[14] Pan and coworkers reported the effect of temperature on the performance of Co_3O_4.[15] Additionally, Boettcher and his group have shown that during alkaline electrolysis, hydroxide anions get adsorbed on the catalyst surface as the major reactant for the OER, and their concentration in the electrolyte determines the overpotential and Tafel slope, *i.e.* activity and kinetics, respectively, of the OER process.[16,17] Besides, certain variables affecting the OER activity of the spinels are the electrolyte, pH, and temperature, which in turn, directly affect the kinetics of the catalytic reaction. Different intrinsic electrochemical parameters like activation energy (E_a), the magnitude of the anodic transfer coefficient (α_a), reaction order (m), *etc.*, determine the individual electrokinetic properties of the catalyst, which collectively hints at the reaction mechanism and kinetics on the catalyst surface. Although Chakraborty and co-workers have demonstrated $SnFe_2O_4$ as a promising bifunctional electrocatalyst for the OER, the role of tetrahedral and octahedral sites, particularly the role of the p-block metal Sn^{II}, and the operating mechanism for the OER on the $SnFe_2O_4$ surface is still conspicuous.

Biswarup Chakraborty

Biswarup Chakraborty is currently an Associate Professor at the Department of Chemistry, Indian Institute of Technology Delhi (IIT Delhi), India, and his research group works on inorganic materials design for photo(electro)catalytic applications, focusing on the structure–activity correlation and establishing the reaction pathway. He did his PhD in inorganic chemistry at the Indian Association for the Cultivation of Science (IACS), India, and completed it in 2014. He then moved to Ben-Gurion University of the Negev, Israel, for postdoctoral research. Before joining IIT Delhi, he had spent more than a year as a postdoctoral fellow at the Technical University of Berlin, Germany.

Herein, two structurally related inverse-spinels, $SnFe_2O_4$ and Fe_3O_4, have been taken as electrocatalysts to perform the alkaline OER, while temperature-dependent electrocatalysis is performed to obtain important intrinsic parameters that can establish the reaction mechanism. The correlation of temperature-dependent and variable concentration studies provides information about the activation energy, reaction order, and the charge transfer coefficient during the OER. Accompanied by the labelling study with D_2O and the kinetic isotope effect (KIE) on the OER, a detailed theoretical study helps to determine the energetics of different reaction steps of the operative AEM for the OER. The introduction of electron-rich Sn in the spinel Fe_3O_4 and its effect on the OER are understood by performing detailed electrokinetics and in-silico studies. In contrast to the extensive experimental studies, theoretical research on the atomistic OER mechanism in spinel oxide catalysts is still rare, which is a prerequisite to designing efficient electrocatalysts. This study thereby addresses the gap through a combined experimental and theoretical study of the OER mechanism on two isostructural spinels, $SnFe_2O_4$ and Fe_3O_4.

Experimental section

Electrokinetic measurements

To study the electrocatalytic activity, a potentiostat (Gamry Interface 1010E) instrument controlled by Echem Analyst™ software was used. The electrochemical study was done in a three-electrode system using a 1 M KOH electrolyte (pH 13.6) where nickel foam (NF) loaded with catalyst was used as a working electrode (WE), a graphite rod was used as a counter electrode (CE) and an Hg/HgO electrode (E° = 0.098 V *vs.* RHE) was used as a reference electrode (RE). CV and LSV were performed to study the electrochemical OER. The manual *iR* compensation (R = resistance of the solution including the test electrode) was 85%, in which the value of uncompensated resistance was obtained from the impedance study. In 1 M KOH, the reference potential with respect to Hg/HgO was converted to potential with reference to the Reversible Hydrogen Electrode (RHE). To study the OER, linear sweep voltammetry (LSV) was performed within a potential range of 1.0 V to 1.8 V (*vs.* RHE) with a scan rate of 1 mV s^{-1}. The obtained polarographs were used to calculate the overpotential at a fixed current density. A temperature-dependent study was performed by varying the temperature from 303 to 343 K. For the temperature-dependent electrochemical study, the cell temperature was recorded with a thermometer dipped into the cell, and the cell was kept in an oil bath to control the temperature. To determine E_a from the temperature-dependent study, the slope of the Arrhenius plot of j_0 *vs.* temperature was found, and the apparent electrochemical activation energy (E_a) was calculated using the Arrhenius relation:

$$\frac{d\ln(i_0)}{d\left(\frac{1}{T}\right)} = -\frac{E_a}{R} \quad (1)$$

where E_a is the activation energy, R is the gas constant, and T is the absolute temperature. Furthermore, the change in the rate of the reaction when moving from lower to higher temperatures was calculated using the Arrhenius formula. The charge transfer coefficient (α) can be determined from the temperature dependence of the Tafel slope according to the following relationship.[18,19]

$$\eta_{OER} = \frac{2.303RT}{\alpha_a nF}\log\left(\frac{j}{j_0}\right) \quad (2)$$

where R is the gas constant, F is the Faraday constant, and n is the number of transferred electrons in the rate-determining step. For a multistep reaction mechanism, the relationship between symmetry factor (β) and α_a is given using the following equation:[20]

$$\alpha_a = \frac{n-s}{\nu} - r\beta \quad (3)$$

where n is the number of electrons involved in the OER (= 4), r is the electrons involved in the rate-determining step (RDS), s is the number of electrons involved in the reaction steps occurring before the RDS, and ν is the stoichiometric number for the OER (= 1).[21] At a fixed temperature, the electrocatalytic study was also performed at different concentrations of KOH, and the concentration was varied from 0.5 to 2 M. The reaction order m at a constant cell voltage was determined using the equation:

$$m_{[OH^-]} = \left(\frac{\partial \log(j)}{\partial \log[OH^-]}\right)_E = -\frac{\left(\frac{\partial E}{\partial \log[OH^-]}\right)_j}{\left(\frac{\partial E}{\partial \log j}\right)_{pH}} \quad (4)$$

The kinetic isotope effect (KIE) was investigated to identify the RDS of the electrocatalytic OER process. For investigating the KIE, 25% D_2O solution in water was used for the preparation of the KOH solution, and the resultant electrolyte was used for the electrocatalytic OER study. Substitution of a proton with an isotope (D) has a significant effect on the reaction rate due to the two-fold increase in mass.[22] KIE is defined as the ratio of the reaction rate constant when protons are available to the reaction rate constant when deuterium ions are available.

The catalytically inactive alkali and alkali earth metal cations in the electrolyte may affect the activity of the catalyst during the OER. In a different set of experiments, the electrolyte was also varied from 1 M LiOH, 1 M NaOH to 1 M KOH. The double layer capacitance (C_{dl}) of the catalyst was determined by recording the cyclic voltammogram (CV) of each catalyst in a non-faradaic region of 0.8953 V to 0.9953 V (*vs.* RHE) in 1 M KOH at varying scan rates (*i.e.*, 10, 25, 50, 100, 150, and 200 mV s^{-1}). To determine C_{dl}, the charging current was measured from each redox half of the CV curve at midway potential, which was then plotted against the scan rate to obtain a linear slope. This slope represents C_{dl} at the electrode–electrolyte interface.

The free energy change in these electrochemical oxidation reactions (*i.e.*, the adsorption-free energies of intermediates) has been calculated using the equation proposed by Nørskov and co-workers.[23]

$$\Delta G = \Delta E + \Delta E_{ZPE} - T\Delta S - neU \quad (5)$$

where ΔE represents the reaction (adsorption) electronic energy computed using DFT; ΔE_{ZPE} denotes the difference in zero-point energies; ΔS is the entropy change obtained from standard tables for gas-phase molecules (NIST database). The term 'e' refers to the charge of an electron, and U is the electrode potential relative to the reversible hydrogen electrode (RHE) model.

Results and discussion

The cubic phase inverse spinel-type $SnFe_2O_4$ and Fe_3O_4 were synthesized by a well-established method using the appropriate stoichiometry of metal salts. The crystallinity of $SnFe_2O_4$ and Fe_3O_4 has been confirmed by PXRD and other spectro/microscopic techniques.[10] The major PXRD reflections were assigned according to JCPDS 11-0614, which confirmed the presence of a cubic phase with the space group $Fd\bar{3}m$ (Fig. 1a). The bulk morphology and size of the catalysts were viewed through high-resolution transmission electron microscopy (HR-TEM). The $SnFe_2O_4$ particles appeared as irregular fragments with an average size of *ca.* 5 nm (Fig. 1b) and the exposed (311) plane with an interplanar distance of 0.25 nm (Fig. 1b inset). The bulk morphology and composition of the as-synthesized $SnFe_2O_4$ particles were verified by field emission scanning electron microscopy (FESEM) imaging and

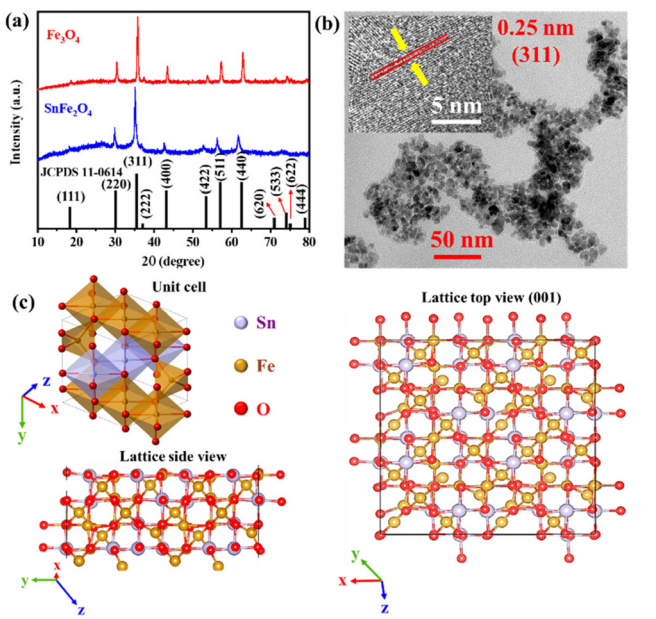

Fig. 1 (a) PXRD pattern of as-synthesized $SnFe_2O_4$ and Fe_3O_4. (b) HRTEM images of $SnFe_2O_4$ along with atomic fringes for the exposed planes in the inset. (c) A polyhedral unit cell of the $SnFe_2O_4$ lattice and the 2 × 2 supercell of the $SnFe_2O_4$ layer showing top and side views of the lattice.

FESEM-energy dispersive X-ray (EDX) elemental mapping. The bulk morphology shows randomly agglomerated semi-spherical nanoparticles (Fig. S1a–S1c†). The FESEM-EDX elemental mapping indicated that composite elements are uniformly distributed over the surface of the catalyst (Fig. S1d–S1f†). The FESEM-EDX elemental ratio for Sn : Fe was also found to be ~1 : 2, whereas O was found to exceed slightly the expected ratio which is possibly due to the surface adsorbed O from the air (Fig. S1g†). The crystal lattice of inverse spinel $SnFe_2O_4$ is composed of $[Sn^{II}O_6]_{Oh}$, $[Fe^{III}O_6]_{Oh}$, and $[Fe^{III}O_4]_{Td}$ units, where $[Sn^{II}O_6]_{Oh}$ occupies half of the octahedral sites, while $[Fe^{III}O_6]_{Oh}$ and $[Fe^{III}O_4]_{Td}$ occupy another half of octahedral and tetrahedral sites, respectively (Fig. 1c). The adjoining multiple-unit cells along the three axes of the cell build up the bulk structure (Fig. 1c). The (001) surface can be created by placing a 2 × 2 supercell of $SnFe_2O_4$ layers. The side or top view of the (001) surface points out that the $[Sn^{II}O_6]_{Oh}$ and $[Fe^{III}O_6]_{Oh}$ sites are exposed on the surface and positioned alternatively to each other *via* μ_2-oxo bridging. In the case of the isostructural ferrite Fe_3O_4 (001) surface, $[Sn^{II}O_6]_{Oh}$ sites will be replaced by the $[Fe^{II}O_6]_{Oh}$ sites.[6–9]

Temperature-dependent OER and activation energy (E_a)

During the OER-LSV study at room temperature (303 K), the polarization curve of the cathodic scan with $SnFe_2O_4$/NF and Fe_3O_4/NF displayed a large current density (j > 300 mA cm^{-2}) at the switching potential (Fig. 2a and S2a†). At a current density of 10 mA cm^{-2}, $SnFe_2O_4$ showed an overpotential (η) of 285 mV, while the reference material Fe_3O_4 showed a larger overpotential of 301 mV (Fig. 2a and S2a†). The effect of temperature on the electrocatalytic OER activity was studied in a 1 M KOH electrolyte with a temperature variation from 303 to 343 K (30 to 70 °C) (Fig. 2a). The effect of temperature on $SnFe_2O_4$/NF was compared with Fe_3O_4/NF as a control material (Fig. S2†). Upon examining the effect of temperature on the OER activity of the catalysts, it could be established that η is inversely proportional to an increase in temperature (Fig. S3†). A plot between overpotential (η) *vs.* $1/T$ at different higher current densities of 10, 50, 100, and 200 mA cm^{-2} shows that a linear relationship holds for Fe_3O_4 at all temperatures, while for $SnFe_2O_4$, a deviation from the linear relationship could be observed (Fig. S3a and S3b†). At a high current of 200 mA, a higher slope of 216 V K for $SnFe_2O_4$ indicates greater dependence of $SnFe_2O_4$ activity on the temperature (Fig. S3c†). The exchange current density (j_0@V ≈ 1.23 V *vs.* RHE) at different temperatures was calculated from the experimental LSV curves. The E_a values of both catalysts were found using eqn (1). The E_a value of Fe_3O_4 turns out to be 3 times larger than that of $SnFe_2O_4$ (Fig. 2b and S2a inset†). For $SnFe_2O_4$, an E_a value of 28.71 kJ mol^{-1} was comparable to other reports like 25 ± 12 kJ mol^{-1} for $NiFeO_x$,[24] while it is considerably lower than 75 kJ mol^{-1} reported for spinel $NiCo_2O_4$ by Davidson *et al.*[25]

E_a can be further used to find the change in the rate of the reaction upon varying the temperature. The increase in the rate of the reaction on moving from 303 K to 343 K was 3.7 times, clearly exhibiting the role of temperature in improving the activity of $SnFe_2O_4$. With the increase in temperature, the charge transfer resistance (R_{ct}) decreases, while it is shown to increase below −10 °C to such an extent that R_{ct} becomes a predominant factor during an electrochemical reaction.[26] Upon increasing the temperature, the R_{ct} value decreases in the case of $SnFe_2O_4$ as well as Fe_3O_4, but the effect was more pronounced in the case of $SnFe_2O_4$, with a decrease of 1.81 Ω, while only 1.00 Ω for Fe_3O_4 (Fig. S4†).

The Raman study done after OER-LSV of $SnFe_2O_4$ and Fe_3O_4 at 343 K showed that the prominent Raman peak at 672 cm^{-1} corresponding to the (A_{1g}) mode of spinels is retained, and no new phase could be observed (Fig. 3f and S6d†). In an earlier report on $NiCo_2O_4$ by Zhou *et al.*, it was found that the Raman spectra or the structure of the catalyst was unchanged after 45 °C until the potential was not increased.[27] Similarly, Zhang *et al.* found spinel Co_3O_4 to be structurally stable up to 75 °C during the oxygen evolution reaction.[15] It is found that at lower potentials, the spinel structures serve as the active species of the OER,[10,27] unlike the electrochemically (*in situ*) formed oxyhydroxide active phases in other transition metal-based catalysts.[28–30]

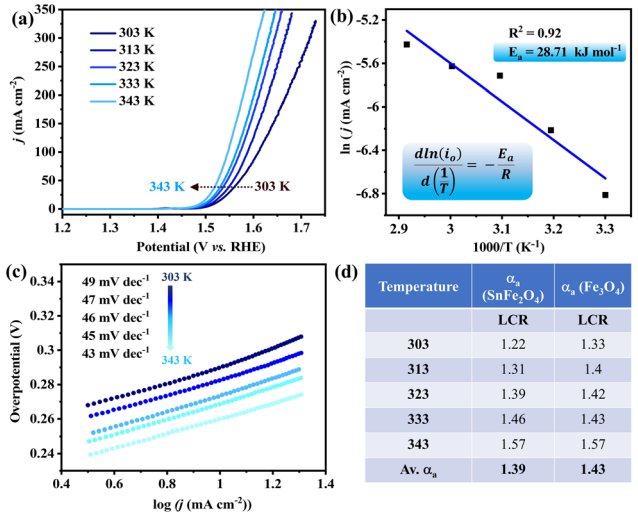

Temperature	α_a ($SnFe_2O_4$)	α_a (Fe_3O_4)
	LCR	LCR
303	1.22	1.33
313	1.31	1.4
323	1.39	1.42
333	1.46	1.43
343	1.57	1.57
Av. α_a	1.39	1.43

Fig. 2 (a) Temperature-dependent OER in 1 M KOH (scan rate 1 mV s^{-1}) catalyzed by $SnFe_2O_4$. (b) ln(j_0) *vs.* 1000/T plot to determine the activation energy of the reaction catalyzed by $SnFe_2O_4$. (c) Tafel slope values for $SnFe_2O_4$ in 1 M KOH over the temperature range of 303–343 K. (d) Table showing the value of the anodic transfer coefficient (α_a) calculated from Tafel slope values for $SnFe_2O_4$ and Fe_3O_4.

Tafel analysis and charge transfer coefficient (α_a)

The Tafel slope values of the OER within the temperature range of 303–343 K were calculated according to eqn (2). The average Tafel slope of 46 ± 3 mV dec^{-1} for $SnFe_2O_4$ signifies peroxide bond formation as the RDS and 2 electron transfer before this electrochemical step;[31] alongside, a small variation of the Tafel slope by 6 mV dec^{-1} upon temperature variation indicates that the RDS does not change with the temperature (Fig. 2c). The Tafel slope value for $SnFe_2O_4$ decreased from

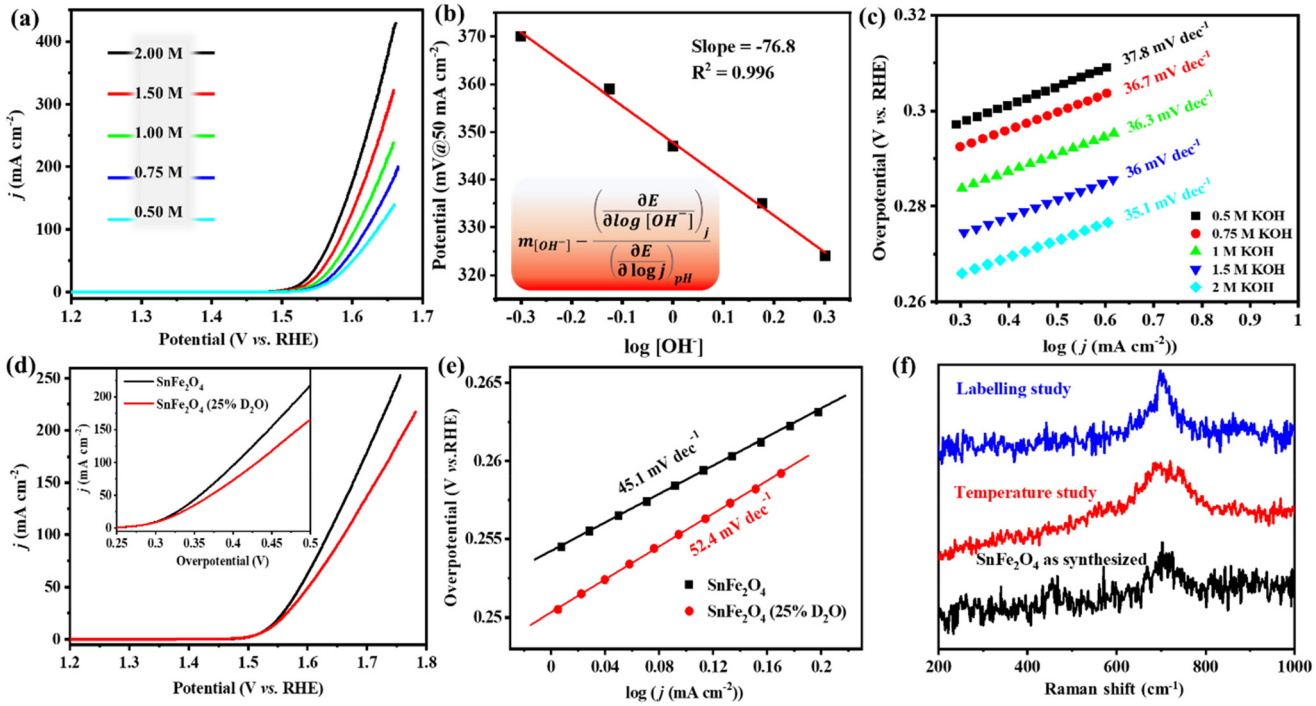

Fig. 3 (a) Polarization curves obtained at variable concentrations of the electrolyte from 0.5 to 2 M KOH (scan rate 1 mV s^{-1}) for $SnFe_2O_4$. (b) Plot of the overpotential *vs.* logarithmic of hydroxide concentration at a constant current. The slope of the linear fit divided by the Tafel slope gives the reaction order (*m*). (c) Corresponding Tafel slope at the variable concentrations of the electrolyte from 0.5 to 2 M KOH. (d) Polarization curves for $SnFe_2O_4$ in the presence of 1 M KOH in 100% H_2O and 1 M KOH in 25% D_2O. (e) Tafel slopes for $SnFe_2O_4$ in the presence of 1 M KOH in 100% H_2O and 1 M KOH in 25% D_2O. (f) Comparative Raman spectroscopic study of as prepared $SnFe_2O_4$, after the temperature-variation study, and after the deuterium labeling study.

49 mV dec^{-1} (at 303 K) to 43 mV dec^{-1} (at 343 K), which was three times higher than Fe_3O_4, which shows a change of only 2 mV dec^{-1} on moving from 303 to 343 K (Fig. 2c and S2b†). These results indicate a greater kinetic dependence of $SnFe_2O_4$ activity on temperature. Another kinetic parameter, *i.e.* α, the fraction of potential at the electrode–electrolyte interface, is used to increase the rate of the reaction by lowering the energy barrier of the reaction. Specifically, during the OER, α can be replaced by an anodic charge transfer coefficient (α_a), which can be related to the Tafel slope. α_a was calculated at the individual temperature in the low current regions (LCR). The average value of $\alpha_a = 1.35 \pm 0.04$ was calculated for $SnFe_2O_4$, while 1.4 ± 0.03 was calculated for Fe_3O_4, respectively (Fig. 2d). The knowledge of α_a also enables the determination of the symmetry factor β according to eqn (3).[19]

Effect of [OH^-] and order of the reaction (*m*)

The change in the reactant concentration at a constant voltage determines the reaction order (*m*). To elucidate the order of the OER (*m*) in the case of $SnFe_2O_4$ and Fe_3O_4, OER-LSV was performed in varying concentrations of KOH solution (Fig. 3a and S5a†). The water activity ([OH^-]) was varied between 0.5 M and 2 M, and the OER polarization curves were recorded at 303 K. The *m* value was determined using eqn (4), where the denominator part of the equation is the Tafel slope, and the numerator part is the slope shown in Fig. 2b and c. With a decrease in the reactant, [OH^-], the cell voltage increased, and the limiting current density decreased (Fig. 3a). The logarithmic plots of the overpotential at high current against the logarithmic [OH^-] gave a slope of −76.8, yielding a reaction order of ~2 for $SnFe_2O_4$ (Fig. 3b) while ~1 for Fe_3O_4 (Fig. S5b†).[12] In the case of $SnFe_2O_4$ as well as Fe_3O_4, concentration-dependent Tafel slopes have a linear relationship with an increase in [OH^-], and a small change in the Tafel slope from 0.5 M KOH to 2 M KOH indicates that the RDS essentially remains the same, with the numerator part being constant in eqn (4) (Fig. 3c and S5c†).

Kinetic isotope effect (KIE) and involvement of protons in the RDS

The difference in the vibrational energies of H and D bonds gives rise to the KIE. The OER-LSV curves of $SnFe_2O_4$ and Fe_3O_4 were studied in a 1 : 4 :: D_2O : H_2O mixture of 1 M KOH, and the LSV polarogram was compared with the OER-LSV curve in 1 M KOH (Fig. 3d and S6a†). The KIE was calculated for $SnFe_2O_4$ and Fe_3O_4 in the overpotential ranges of 0.35–0.45 mV and 0.35–0.4 mV, respectively (Fig. S6c†). The variation of the isotope effect (IE) with varying potentials indicates that the IE is a kinetic phenomenon.[32] The KIE of $SnFe_2O_4$ and Fe_3O_4 yielded average values of 1.29 and 3.5, respectively. The obtained value ($1 < KIE < 2$) for $SnFe_2O_4$ signifies the secondary KIE where the RDS does not directly

involve the breaking of the D–O/H–O bond, while a higher value (2 < KIE < 7) in the case of Fe_3O_4 indicates the primary KIE, *i.e.*, the bond involving the isotope (D) is being formed or broken.[22] In Fe-containing catalysts, the decrease in the OER activity accompanied by an increase in the Tafel slope during alkaline OER in deuterated water may be due to the effect on the interactions of intermediates with adsorbed water. The increase in the Tafel slope observed for $SnFe_2O_4$ as well as Fe_3O_4 on moving from H_2O to D_2O indicates the variation in the enthalpy of formation of the intermediate in the RDS, *i.e.*, the interaction between $*O\cdots HO^-$ (the formation of O–O bond) (Fig. 3e and S6b†).[33] The exchange of hydrogen with deuterium does not significantly affect the electronic structure or the energetics of the catalyst surface. It primarily affects the reaction rates rather than the surface of the catalyst. To validate this fact, the Raman study of $SnFe_2O_4$ and Fe_3O_4 was done after OER-LSV at 343 K, and the structure of the catalysts was found to be unchanged after the KIE study (Fig. 3f and S6d†).

Effect of the electrolyte cation on the OER activity

The OER-LSV curves of Fe_3O_4 and $SnFe_2O_4$ were recorded in 1 M KOH, NaOH, and LiOH, where the metal ions K^+, Na^+, and Li^+, respectively, have ionic radii of 1.38 Å, 1.02 Å, and 0.76 Å (Fig. 4a and b). In the case of $SnFe_2O_4$, a significant anodic shift in the onset potential of *ca.* 100 mV was observed from KOH to LiOH, accompanied by a decrease in the limiting current value. As the size of alkali metal cations decreases, the overpotential increases in the order, KOH (282 mV), NaOH (327 mV), and LiOH (380 mV), which leads to the conclusion that bigger cations help in enhancing the OER activity (Fig. 4a). A similar trend of activity was previously observed in the literature.[34,35] The choice of metal ions in the electrolyte affects the OER process in terms of the electrochemical surface area (ECSA), reaction mechanism, intermediate formation, kinetics, *etc.* Boettcher and co-workers found out that during the OER on the NiO(OH) surface, other alkali earth metals like Mg^{2+} and Ca^{2+} in the electrolyte were found to inhibit the activity due to their higher Lewis acidity and strong affinity towards the OER intermediates.[34] It is assumed that the electrolyte cation interacts with the peroxo species formed during the acid–base reaction step of the OER process, as shown below:[36]

$$M\text{–}OO\text{–}H + C^+ \leftrightarrow M\text{–}OO^-\text{–}C^+ + H^+$$

where M represents the active metal centre of the catalyst and C^+ represents the metal cation in the electrolyte. The non-covalent interaction between the metal cations in the electrolyte and the adsorbed species on the electrode surface may provide stabilization to the intermediate peroxo species, with bigger cations (K^+ in this study) providing better stabilization.[37] According to a theoretical study by Boettcher and co-workers, among K^+ and Na^+, the distance of the M–O bond ($Na^+\cdots OH^-$) is shorter than that of KOH, accompanied by the less O-centered Bader charge in the case of K–O, thereby weak-

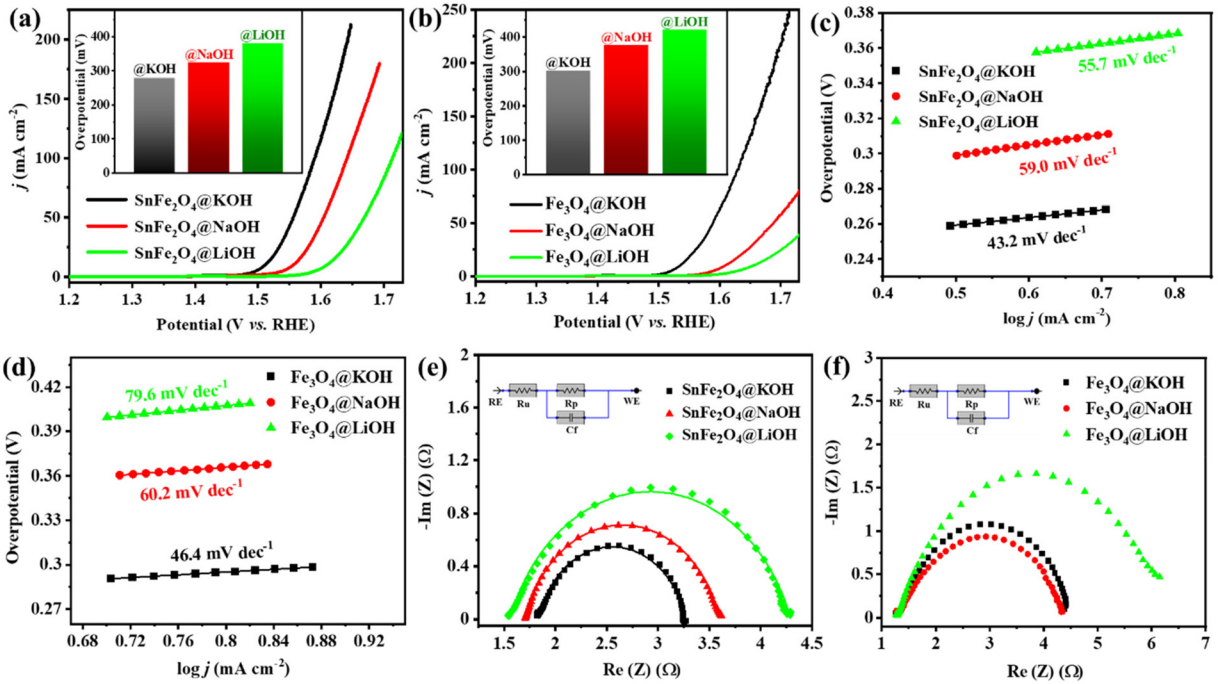

Fig. 4 (a) Polarization curves of $SnFe_2O_4$ recorded with 1 M KOH, NaOH, and LiOH electrolytes (scan rate 1 mV s^{-1}). The inset shows a bar plot of the overpotential (@ 10 mA cm^{-2}) *vs.* electrolyte. (b) Polarization curves of Fe_3O_4 in 1 M KOH, NaOH, and LiOH (scan rate 1 mV s^{-1}). The inset shows a bar plot of the overpotential (@ 10 mA cm^{-2}) *vs.* electrolyte. Corresponding Tafel plots in 1 M KOH, NaOH, and LiOH for (c) $SnFe_2O_4$ and (d) Fe_3O_4. A Nyquist plot from the EIS data obtained in 1 M KOH, NaOH, and LiOH for (e) $SnFe_2O_4$ and (f) Fe_3O_4. The inset shows the equivalent circuit fitting (R_u = R_s = solvent resistance; R_p = R_{ct} = charge transfer resistance; and C_f = C_{dl} = double layer capacitance).

ening the K–O bond and allowing more water molecules to interact with the adsorbed species on the catalyst surface and boosting the OER.[34] This again explains the less OER overpotential in the 1 M KOH electrolyte. The Tafel slopes calculated for $SnFe_2O_4$ as well as Fe_3O_4 in various electrolytes came in the order KOH < NaOH < LiOH, where the least Tafel slopes of 43.2 mV dec^{-1} and 46.4 mV dec^{-1} were displayed in 1 M KOH for $SnFe_2O_4$ and Fe_3O_4, respectively (Fig. 4c and d).[32,38] The lower Tafel slope in the case of KOH can be attributed to the weak $K^+\cdots OH^-$ bonding, which promotes the OH_{ads} dissociation and O_{ads} adsorption and accelerates the reaction kinetics (ads = adsorbed).[39] The order of the Tafel slope also concludes that the ionic resistance decreases, and in turn, the transport of interfacial OH^- intermediates increases in the order of KOH > NaOH > LiOH.

The resistance in various electrolytes can also be verified by the electrochemical impedance study (EIS) done with $SnFe_2O_4$ and Fe_3O_4 in 1 M each of KOH, NaOH, and LiOH. EIS was also used to determine the capacitance value by the fitting of the equivalent circuits. The EIS study was performed for $SnFe_2O_4$ in KOH, NaOH, and LiOH at fixed potentials of 1.54 V, 1.58 V, and 1.62 V (*vs.* RHE), respectively, and the low-frequency impedance increased in the order, Li > Na > K (Fig. 4e). The charge transfer resistance of the catalyst was the least in the case of KOH (1.9 Ω), followed by NaOH (2.4 Ω) and LiOH (2.66 Ω). The constant phase element (CPR) model was used to fit the corresponding circuits since it also represents the capacitor (double layer) formed at the electrode–electrolyte interface (Fig. 4e inset). The double layer capacitance (C_{dl}), which is a way to evaluate the electrochemically active surface area, was calculated using the R_{ct} value from the CPE fitting (Fig. S7†). The maximum C_{dl} value of 9.05 mF was attained for $SnFe_2O_4$ in 1 M KOH, which is also validated by the C_{dl} values obtained by the CV cycles in non-faradaic regions (Fig. S8†). As anticipated, the highest C_{dl} value of 0.86 mF was obtained for $SnFe_2O_4$ in 1 M KOH and a comparable C_{dl} in NaOH and LiOH using the cyclic voltammetry curves in the non-faradaic region (Fig. S8†). A similar trend of impedance and C_{dl} was observed in the case of Fe_3O_4 in 1 M each of KOH, NaOH, and LiOH (Fig. 4f and S9†).

DFT study

DFT calculations were carried out within the (001) plane using a 2 × 2 supercell of inverse spinel $SnFe_2O_4$ (a = 17.44 Å, b = 17.44 Å, c = 30.00 Å, and $\alpha = \beta = \gamma = 90°$) (Fig. 1c) to study the OER kinetics. The oxygen evolution reaction (OER) is comprised of the following four elementary steps, each involving the transfer of an electron until OH^- is oxidized to water (H_2O).[23,40]

$$OH^- + * \rightarrow *OH + e^- \quad (1)$$

$$*OH + OH^- \rightarrow *O + H_2O + e^- \quad (2)$$

$$*O + OH^- \rightarrow *OOH + e^- \quad (3)$$

$$*OOH + OH^- \rightarrow * + H_2O + O_2 + e^- \quad (4)$$

Here, * represents the active sites on the surface of the electrocatalyst (in this case, an inverse spinel). The adsorption of OH^- and the formation of OER intermediates on the (001) surface of $SnFe_2O_4$ is shown in Fig. 5. The reaction in an alkaline medium commences by direct adsorption of OH^- ions on Fe sites to form *OH by one e^- oxidation (step I). In the second step, another OH^- group attacks, and accompanied by the coupled H^+ and e^- removal, the *O intermediate is formed at the bridging sites of the $SnFe_2O_4$ surface (step II). The *O intermediate is typically positioned between two surface atoms (Sn and Fe) at the active site. In the third step, the *OOH (hydroperoxyl) intermediate forms after the attack of another OH^-. The *OOH molecule is also adsorbed on top of the surface, suggesting a direct interaction with the surface Sn and Fe atoms at the active site. Finally, the reaction with another OH^- leads to the formation of O_2 and H_2O.

The active site preference during alkaline OER was compared between Fe_3O_4 and $SnFe_2O_4$ spinels. The energy profile diagram (Fig. 5) illustrates an OER pathway at 0 V, 1.23 V, and

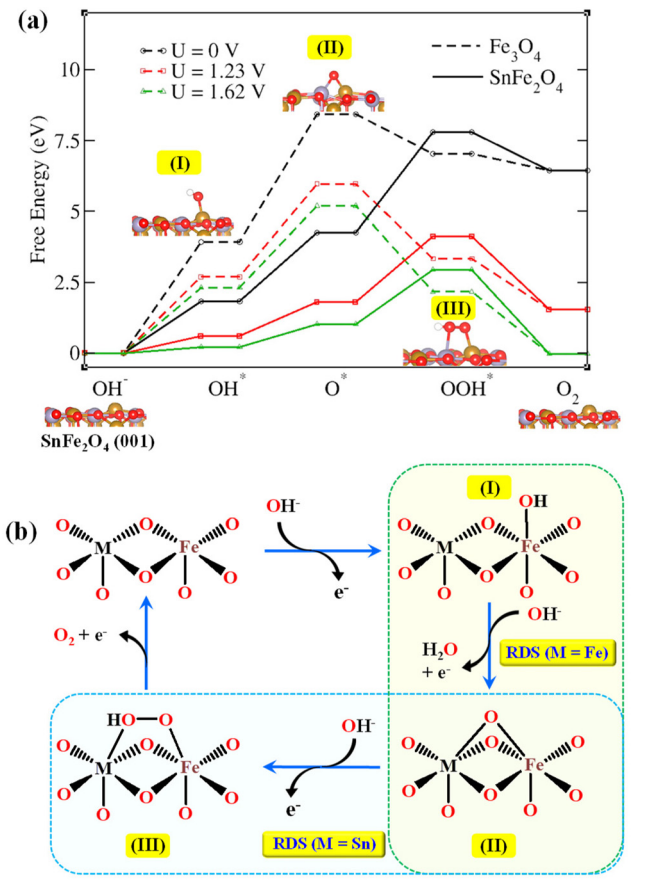

Fig. 5 (a) The free energy diagram of the OER of the $SnFe_2O_4$ (solid line) and Fe_3O_4 (dotted line) on the (001) surface at potentials of U = 0 V (black line), 1.23 V (red line), and 1.62 V (green line) (*vs.* RHE). Shown below are the optimized OER intermediates on the $SnFe_2O_4$ (001) surface. Colour code: brown balls = Fe; red balls = O; and gray balls = Sn. (b) Schematic representation of the OER mechanism under alkaline conditions facilitated by the synergistic action of M–μ_2-O–M metal atoms.

1.62 V, the OER overpotential, where the adsorption-free energies of intermediates were calculated using eqn (5). Between $SnFe_2O_4$ and Fe_3O_4, the lowest overall OER free energy change was shown by $SnFe_2O_4$ at different potentials (Table S1†). In the case of $SnFe_2O_4$, the energetically uphill reaction step, or the RDS, leads to the formation of *OOH, with endothermic free energy of 1.93 eV for an applied overpotential of 1.62 V.[41] Fe_3O_4 exhibits a higher overall OER free energy change with endothermic free energy of 2.89 eV for its rate-determining step of *O formation with an applied overpotential of 1.62 V.

Proposed OER mechanism

The OER is a complex multistep reaction. After prolonged experimental and computational studies, three different OER intermediates, namely O_{ads}, OH_{ads}, and OOH_{ads}, have been identified during the catalytic mechanism. Rossmeisl *et al.*[42] performed DFT calculations for rutile RuO_2, IrO_2, and TiO_2. The DFT calculations considered the concerted proton-coupled electron transfer (PCET) steps, *i.e.*, one H^+ and one e^- are transferred in a single kinetic step. Contrary to other mechanisms,[43] Rossmeisl's peroxide path (RPP) involves peroxide formation in the third step due to a lesser activation barrier than the direct formation of O_2 from O_{ad}.[42,44] For a multistep reaction, the overall rate of the reaction is limited to the rate of its slowest step, and the overall rate cannot exceed the rate of the slowest step. Generally, during heterogeneous electrocatalytic reactions, the reaction step involving a single intermediate species and a single type of active site is considered to be the RDS. Either the deprotonation of OH_{ads} ($OH_{ads} = O_{ads} + H^+ + e^-$) or the O–O bond formation ($O_{ads} + OH^- = OOH_{ads} + e^-$) is often found to be the RDS for heterogeneous systems.[45] From the results of the calculated Tafel slope (46 ± 3 mV dec^{-1}) over a temperature range and a reaction order close to 2, the RDS of the metal peroxo bond can be acknowledged. The results of the symmetry factor also complement the hypothesis that step 3 of RPP, *i.e.* metal peroxo bond, is the rate-determining step of $SnFe_2O_4$.

To understand the improved OER activity of $SnFe_2O_4$ in comparison with Fe_3O_4, DFT calculations were carried out to understand the atomic scale OER mechanism on the Fe active sites of the (001) surface (Fig. 5a and S10a†). The adsorbed intermediates during the OER, *i.e.*, *OH, *O, and *OOH are stabilized on the (001) catalyst surface by hydrogen bonding with solvent water molecules. The OER process on Fe_3O_4 (001) was limited by the oxidation of *OH to *O, perhaps due to the weak binding between *O and Fe atoms (Fig. 5b and S10b†). Replacing Fe^{II} with Sn^{II} ions in the Fe_3O_4 lattice improves the OER activity of the (001) surface of $SnFe_2O_4$ due to the synergistic effect of Fe and Sn in stabilizing the OER intermediates. As a consequence, the rate-limiting step for $SnFe_2O_4$ changes to the conversion of *O to *OOH (Fig. 5b). The formation of OOH* on the $SnFe_2O_4$ surface is an endothermic process ($\Delta H_f = 3.547$ eV) and is facilitated by the applied potential during the electrochemical OER. The direct involvement of the isotopically labelled species in the RDS of Fe_3O_4, *i.e.*, the deuteration of *OD to form *O, was supported by the primary KIE shown by Fe_3O_4. Moreover, the secondary KIE shown by $SnFe_2O_4$ supported the indirect involvement of O–H/O–D in the RDS.

From the literature studies, it is evident that for spinel ferrites, the (001) surface is most suited for the OER DFT study. Piccinin and coworkers found that on the (001) surface of Fe_3O_4, both terminal oxygen and bridging oxygen atoms can participate in the OER. While considering the distorted bulk truncated (DBT) model, the OER in Fe_3O_4 was found to proceed *via* the terminal oxygen, and the RDS was the dehydrogenation of the *OH group. Upon considering the subsurface cation vacancy (SCV) model, the OER proceeded *via* the bridging oxygen, and the RDS was the formation of the hydroperoxo species.[40] Similarly, a DFT study was performed to understand the OER process on the (001) surface of inverse spinel $NiFe_2O_4$ and $CoFe_2O_4$. For $NiFe_2O_4$, Fe is the main catalytic site where the OER happens preferably by the LOM pathway with O–O as the RDS. In the case of $CoFe_2O_4$, Co and Fe can participate in the OER as the active catalytic site. Fe-site favoured the LOM pathway whereas the Co sites preferred the AEM pathway, thus concluding the coexistence of two active sites in $CoFe_2O_4$.[6] Likewise, in a DFT study performed by Peng *et al.* on spinel undoped, and Fe- and Ni-doped Co_3O_4 (001) surfaces, the octahedral Co sites were found to be OER active in all cases. However, the RDS changed from *OH formation in the case of Ni-doped Co_3O_4 to *OOH formation in the case of Fe-doped Co_3O_4.[46] Interestingly, unlike other metal ferrites, where individual metal sites can act independently in assisting the catalytic OER, in the case of $SnFe_2O_4$, Fe^{III} and Sn^{II} act in synergy to facilitate the OER on the (001) surface.

Conclusion

Currently, the rational design of electrocatalysts for the OER is limited by the vague understanding of the in-depth kinetic analysis and reaction mechanism, particularly for the OER. In this research, the experimental results, coupled with the computational modelling, could enlighten a path to the detailed understanding and designing of the electrocatalysts, eventually leading to a more efficient electrocatalytic OER. As a contribution towards understanding the OER on the spinel surface and the role of heteroatom substitution in the lattice, the reaction mechanism and electrokinetic parameters were studied on two isostructural inverse spinels, $SnFe_2O_4$ and Fe_3O_4. The experimentally obtained E_a values from the temperature-dependent study of $SnFe_2O_4$ and Fe_3O_4 suggest that the substitution of Fe^{II} with Sn^{II} in the Fe_3O_4 lattice decreases the activation energy of the OER by as much as three times. Alongside, the reaction order also changed from 2 in the case of $SnFe_2O_4$ to 1 in the case of Fe_3O_4. These experimental findings were the primary evidence of the change in the RDS during the OER as a result of the substitution of Fe^{II} by a heteroatom in the catalyst lattice. A slight change in the Tafel slope with temperature in the case of $SnFe_2O_4$ and Fe_3O_4 substantiated that the rate-determining step, albeit different, was

independent of the change in the cell temperature. The DFT study on the (001) surface of $SnFe_2O_4$ and Fe_3O_4 validated that the reaction on both catalysts was limited to the AEM pathway, which was also supported by the experimentally determined intrinsic parameters. On the (001) surface of Fe_3O_4, the formation of *O was the rate-limiting step, while on $SnFe_2O_4$, the metal-peroxo (*OOH) formation became the RDS. From the current research, it can be discerned that the presence of a heteroatom in the spinel ferrite may drastically affect the reaction pathway and, hence, the RDS during the electrocatalytic OER. Conclusively, the change in the reaction mechanism and the RDS upon p-block metal doping in Fe_3O_4 is the key finding. Therefore, analysis of the role of each catalytic site during the reaction mechanism is critical for engineering the catalyst to further enhance its OER efficiency. Unlike other DFT-modelled spinel catalysts, where individual 3d transition metal centres act independently to catalyze the OER, the Fe^{III}_{Oh} centre in inverse-spinel $SnFe_2O_4$ acts synergistically with the Sn^{II}_{Oh} unit to facilitate the catalytic OER.

Data availability

Characterization of the catalysts by spectroscopic, microscopic, PXRD, and analytical techniques along with the details of the experimental and electrochemical methods are included in the ESI.†

Conflicts of interest

There are no conflicts to declare.

Acknowledgements

AR sincerely acknowledges the PMRF scheme of the Gov. of India (ID 1401195) for the fellowship. BC sincerely acknowledges the IIT Delhi seed grant PLN12/04CY. The authors thank the Central Research Facility-IIT Delhi for the microscopic and XPS facilities. PS and PKS acknowledge the computational facilities in the Department of Chemistry at BITS Pilani (Hyderabad campus).

References

1 R. J. Hill, J. R. Craig and G. V. Gibbs, *Phys. Chem. Miner.*, 1979, **4**, 317–339.
2 Y. Sun, J. Wang, S. Xi, J. Shen, S. Luo, J. Ge, S. Sun, Y. Chen, J. V. Hanna, S. Li, X. Wang and Z. J. Xu, *Nat. Commun.*, 2023, **14**, 2467.
3 C. Wei, R. R. Rao, J. Peng, B. Huang, I. E. L. Stephens, M. Risch, Z. J. Xu and Y. Shao-Horn, *Adv. Mater.*, 2019, **31**, 1806296.
4 Y. Zhou, S. Sun, C. Wei, Y. Sun, P. Xi, Z. Feng and Z. J. Xu, *Adv. Mater.*, 2019, **31**, 1902509.
5 S. Sun, Y. Sun, Y. Zhou, S. Xi, X. Ren, B. Huang, H. Liao, L. P. Wang, Y. Du and Z. J. Xu, *Angew. Chem., Int. Ed.*, 2019, **58**, 6042–6047.
6 Ö. N. Avcı, L. Sementa and A. Fortunelli, *ACS Catal.*, 2022, **12**, 9058–9073.
7 V. Jeyavani, S. Manoj and S. P. Mukherjee, *ACS Appl. Nano Mater.*, 2024, **7**, 17776–17785.
8 Q. Zhang, Y. Hu, H. Wu, X. Zhao, M. Wang, S. Wang, R. Feng, Q. Chen, F. Song, M. Chen and P. Liu, *ACS Nano*, 2023, **17**, 1485–1494.
9 R. Chen, Z. Wang, S. Chen, W. Wu, Y. Zhu, J. Zhong and N. Cheng, *ACS Energy Lett.*, 2023, **8**, 3504–3511.
10 A. Rajput, A. A. Pandey, A. Kundu and B. Chakraborty, *Chem. Commun.*, 2023, **59**, 4943–4946.
11 H. Xiao, H. Shin and W. A. Goddard, *Proc. Natl. Acad. Sci. U. S. A.*, 2018, **115**, 5872–5877.
12 L. Bai, S. Lee and X. Hu, *Angew. Chem., Int. Ed.*, 2021, **60**, 3095–3103.
13 A. G. Rajan, J. M. P. Martirez and E. A. Carter, *ACS Catal.*, 2021, **11**, 11305–11319.
14 B. Chakraborty, A. Indra, P. V. Menezes, M. Driess and P. W. Menezes, *Mater. Today Chem.*, 2020, **15**, 100226.
15 G. Zhang, H. Wang, J. Yang, Q. Zhao, L. Yang, H. Tang, C. Liu, H. Chen, Y. Lin and F. Pan, *Inorg. Chem.*, 2018, **57**, 2766–2772.
16 T. Shinagawa, A. T. Garcia-Esparza and K. Takanabe, *Sci. Rep.*, 2015, **5**, 13801–13822.
17 L. Trotochaud, J. K. Ranney, K. N. Williams and S. W. Boettcher, *J. Am. Chem. Soc.*, 2012, **134**, 17253–17261.
18 E. Fabbri, A. Habereder, K. Waltar, R. Kötz and T. J. Schmidt, *Catal. Sci. Technol.*, 2014, **4**, 3800–3821.
19 T. Schuler, T. Kimura, T. J. Schmidt and F. N. Büchi, *Energy Environ. Sci.*, 2020, **13**, 2153–2166.
20 J. O. M. Bockris and Z. Nagy, *J. Chem. Educ.*, 1973, **50**, 839.
21 L. Negahdar, F. Zeng, S. Palkovits, C. Broicher and R. Palkovits, *ChemElectroChem*, 2019, **6**, 5588–5595.
22 T. Y. George, T. Asset, A. Avid, P. Atanassov and I. V. Zenyuk, *ChemPhysChem*, 2020, **21**, 469–475.
23 J. K. Nørskov, J. Rossmeisl, A. Logadottir, L. Lindqvist, J. R. Kitchin, T. Bligaard and H. Jonsson, *J. Phys. Chem. B*, 2004, **108**, 17886–17892.
24 E. Nurlaela, T. Shinagawa, M. Qureshi, D. S. Dhawale and K. Takanabe, *ACS Catal.*, 2016, **6**, 1713–1722.
25 C. Davidson, G. Kissel and S. Srinivasan, *J. Electroanal. Chem. Interfacial Electrochem.*, 1982, **132**, 129–135.
26 S. Zhang, K. Xu and T. Jow, *J. Power Sources*, 2003, **115**, 137–140.
27 T. Zhou, C. Wang, Y. Shi, Y. Liang, Y. Yu and B. Zhang, *J. Mater. Chem. A*, 2020, **8**, 1631–1635.
28 A. Rajput, P. K. Nayak, D. Ghosh and B. Chakraborty, *ACS Appl. Mater. Interfaces*, 2024, **16**, 28756–28770.
29 A. Rajput, M. K. Adak and B. Chakraborty, *Inorg. Chem.*, 2022, **61**, 11189–11206.
30 M. K. Adak, A. Rajput, D. Ghosh and B. Chakraborty, *ACS Appl. Energy Mater.*, 2022, **5**, 13645–13660.

31 Y. Hao, Y. Li, J. Wu, L. Meng, J. Wang, C. Jia, T. Liu, X. Yang, Z.-P. Liu and M. Gong, *J. Am. Chem. Soc.*, 2021, **143**, 1493–1502.
32 M. K. Adak, L. Mallick, K. Samanta and B. Chakraborty, *J. Phys. Chem. C*, 2023, **127**, 154–168.
33 C. Yang, O. Fontaine, J. M. Tarascon and A. Grimaud, *Angew. Chem.*, 2017, **129**, 8778–8782.
34 J. Zaffran, M. B. Stevens, C. D. Trang, M. Nagli, M. Shehadeh, S. W. Boettcher and M. C. Toroker, *Chem. Mater.*, 2017, **29**, 4761–4767.
35 J. D. Michael, E. L. Demeter, S. M. Illes, Q. Fan, J. R. Boes and J. R. Kitchin, *J. Phys. Chem. C*, 2015, **119**, 11475–11481.
36 A. C. Garcia, T. Touzalin, C. Nieuwland, N. Perini and M. T. Koper, *Angew. Chem., Int. Ed.*, 2019, **58**, 12999–13003.
37 X. Chen, I. T. McCrum, K. A. Schwarz, M. J. Janik and M. T. Koper, *Angew. Chem., Int. Ed.*, 2017, **56**, 15025–15029.
38 A. Kundu, B. Kumar and B. Chakraborty, *J. Phys. Chem. C*, 2022, **126**, 16172–16186.
39 J. A. D. del Rosario, G. Li, M. F. M. Labata, J. D. Ocon and P.-Y. A. Chuang, *Appl. Catal., B*, 2021, **288**, 119981.
40 G. Righi, S. Fabris and S. Piccinin, *J. Phys. Chem. C*, 2021, **125**, 18752–18761.
41 K. S. Exner and H. Over, *ACS Catal.*, 2019, **9**, 6755–6765.
42 J. Rossmeisl, Z.-W. Qu, H. Zhu, G.-J. Kroes and J. K. Nørskov, *J. Electroanal. Chem.*, 2007, **607**, 83–89.
43 J. M. Bockris, *J. Chem. Phys.*, 1956, **24**, 817–827.
44 J. K. Nørskov, T. Bligaard, A. Logadottir, S. Bahn, L. B. Hansen, M. Bollinger, H. Bengaard, B. Hammer, Z. Sljivancanin and M. Mavrikakis, *J. Catal.*, 2002, **209**, 275–278.
45 Y. Duan, N. Dubouis, J. Huang, D. A. D. Corte, V. Pimenta, Z. J. Xu and A. Grimaud, *ACS Catal.*, 2020, **10**, 4160–4170.
46 Y. Peng, H. Hajiyani and R. Pentcheva, *ACS Catal.*, 2021, **11**, 5601–5613.